

## Article

# Effect of 1wt%Zn Addition on Microstructure and Mechanical Properties of Mg-6Er Alloys under High Strain Rates

Hui Yu <sup>1,2,\*</sup>, Junchao Ren <sup>1</sup>, Shaoming Kang <sup>1,2</sup>, Wei Yu <sup>3,\*</sup>, Zhifeng Wang <sup>1</sup> , Jianhang Feng <sup>1,2</sup>, Qingzhou Wang <sup>1,2</sup>, Puguang Ji <sup>1,2</sup>, Xin Zhang <sup>1,2</sup> and Fuxing Yin <sup>1,2,4</sup> 

- <sup>1</sup> School of Materials Science and Engineering, Hebei University of Technology, Tianjin 300130, China; junchaoren@163.com (J.R.); kangdashao@163.com (S.K.); wangzf@hebut.edu.cn (Z.W.); 13933765819@126.com (J.F.); qzwwang@hebut.edu.cn (Q.W.); jipuguang@hebut.edu.cn (P.J.); zhang\_xin@hebut.edu.cn (X.Z.); yinfuxing@hebut.edu.cn (F.Y.)
- <sup>2</sup> Tianjin Key Laboratory of Materials Laminating Fabrication and Interfacial Controlling Technology, Tianjin 300130, China
- <sup>3</sup> Hefei Nova Advanced Materials Company Ltd., Hefei 230091, China
- <sup>4</sup> Institute of New Materials, Guangdong Academy of Sciences, Guangzhou 510651, China
- \* Correspondence: yuhuidavid@hebut.edu.cn (H.Y.); yuwei52213@163.com (W.Y.); Tel.: +86-185-2223-3466 (H.Y.); +86-138-6672-3380 (W.Y.)

**Abstract:** In this study, we investigated the high strain rate response of Mg-6wt%Er alloys with 1wt%Zn addition by split Hopkinson pressure bar (SHPB) tests in a range of 900–2500 s<sup>-1</sup>. Their related microstructures were also characterized by optical microscopy (OM), scanning electron microscopy (SEM), electron back-scattering diffraction (EBSD), and transmission electron microscopy (TEM). In particular, the twinning and stacking faults (SFs) in Mg-6Er and Mg-6Er-1Zn alloys are characterized, and the interactions between twin/SFs and dislocations are analyzed in detail. Compared with twins, the dispersed and dense SFs seem to more readily interact with dislocations, resulting in the enhancement of the strength of alloys. Especially at a high strain rate of 1450 s<sup>-1</sup>, dislocations are prone to tangle around the twins and SFs, forming low-angle grain boundaries (LAGBs). The addition of Zn in Mg-6Er can make LAGBs more easily transform into high-angle grain boundaries (HAGBs) due to the existence of SFs.

**Keywords:** magnesium; high strain rate deformation; stacking faults; microstructure



**Citation:** Yu, H.; Ren, J.; Kang, S.; Yu, W.; Wang, Z.; Feng, J.; Wang, Q.; Ji, P.; Zhang, X.; Yin, F. Effect of 1wt%Zn Addition on Microstructure and Mechanical Properties of Mg-6Er Alloys under High Strain Rates. *Metals* **2022**, *12*, 883. <https://doi.org/10.3390/met12050883>

Academic Editor: Marcello Cabibbo

Received: 27 April 2022

Accepted: 20 May 2022

Published: 23 May 2022

**Publisher's Note:** MDPI stays neutral with regard to jurisdictional claims in published maps and institutional affiliations.



**Copyright:** © 2022 by the authors. Licensee MDPI, Basel, Switzerland. This article is an open access article distributed under the terms and conditions of the Creative Commons Attribution (CC BY) license (<https://creativecommons.org/licenses/by/4.0/>).

## 1. Introduction

As the lightest structural material, magnesium (Mg) alloys have received increasing attention in various industries due to their low density (~1.8 g/cm<sup>3</sup>), high specific strength/stiffness, good heat dissipation, and damping [1]. However, the application of Mg alloy components strictly requires various strain rates under some circumstances [2,3]. In addition to static deformation, Mg products are usually subjected to high-speed impact loads (i.e., shock and collision) [4,5]. Such high-speed deformation of Mg alloys generally leads to unpredictable serious failure in a short time [6]. Therefore, understanding the dynamic response of Mg alloys under high-speed impact loading not only provides more insight for developing high-performance Mg alloys, but also extends the application field in the near future [7].

It is well known that the microstructure of Mg-RE-Zn alloys strongly depends on their composition. In general, three kinds of second phases, namely, long period stack order (LPSO) phase, quasi-crystalline I phase, and W phase, can be introduced depending on various RE/Zn mass ratios [8,9]. In particular, SFs are occasionally found in as-cast or heat-treated Mg-RE-Zn alloys [10], which are usually considered to be the early stages of LPSO transformation [11,12].

Recently, high-performance Mg-RE-Zn alloys with profuse SFs have been reported by the utilization of casting, heat treatment, and hot extrusion [13–17]. For example, Zhang

et al. [13] found that the yield strength of Mg-6Ho-1Zn alloys with large amounts of SFs was much higher than that of Mg-6Ho alloys without SFs. The SF-embedded Mg-4Er-4Gd-1Zn alloy also showed higher strength than that of the Mg-8Er alloy with no SFs [14]. Many studies have focused on the microstructural evolution and mechanical properties of Mg alloys at different loading rates [18–22]. For instance, Wang et al. [18] quantitatively studied the evolution of dislocations and deformation twins at different strain rates in AZ311 alloys. However, the effects of substructure on the mechanical properties of Mg alloys under high strain rates have rarely been reported, especially in Mg alloys with SFs or twins built in.

Thus, in this work, we prepared a Mg-6Er-1Zn alloy (containing SFs) by adding 1wt%Zn to a Mg-6Er alloy (containing twins). We investigated the effects of the Zn addition on the microstructure and mechanical properties of Mg-6Er alloys at high strain rates by dynamic impacting tests, in order to reveal the effects of twins and SFs on magnesium alloys at high strain rates. Meanwhile, more attention is paid to the interaction of dislocations with twinning and SFs under high strain rates by SHPB tests. The present study aims to enrich the dynamic impact theory of Mg alloys and provide technical support for the development of superior Mg alloys in the near future.

## 2. Materials and Methods

Commercially pure Mg (99.9 wt %), pure zinc (99.9 wt %), and a Mg-20Er master alloy were chosen and melted in a resistance furnace at 760 °C under gas protection of SF<sub>6</sub> and CO<sub>2</sub>. The melt was stirred at 720 °C and poured into a stainless steel mold preheated to 200 °C. Finally, the ingots of Mg-6Er and Mg-6Er-1Zn alloys, with a diameter of 60 mm and a height of 150 mm, were cast and machined, then preheated at 400 °C for 30 min. The extrusion of billets was carried out at 400 °C with an extrusion ratio of 25:1 and extrusion speed of 1 mm/s.

Cylindrical specimens with the dimensions  $\phi 8 \times 12$  mm and  $\phi 8 \times 5$  mm were cut from the extrusion bar along the extrusion direction (ED) for quasi-static compression tests and dynamic impact tests, respectively. The dog bone tensile specimens with a gauge length of 25 mm and a cross-section of 5 mm were examined according to the GB/T228.1-2010 standard. Quasi-static compression and tension tests with a strain rate of 0.001 s<sup>-1</sup> were performed at room temperature using a universal testing machine (SUNS UTM5105G, SUNS, Shenzhen, China). Dynamic impact experiments were carried out by SHPB (Archimedes ALT1000, Archimedes, Beijing, China). Figure 1 shows the schematic experimental procedure and typical raw data (i.e., incident, transmitted, and reflected curves) recorded. The dynamic impact tests were performed at room temperature with impact velocity of the strike bar of 4–10 m/s and an impact strain rate of 900–2500 s<sup>-1</sup>. The dynamic mechanical parameters of the specimens could be calculated indirectly from the data recorded by the strain gauges [23].

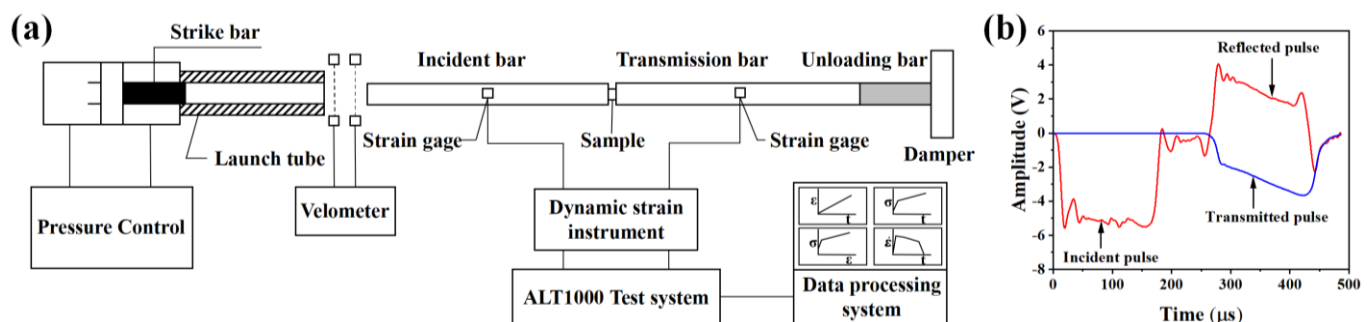


**Figure 1.** (a) Schematic diagram of the split Hopkinson pressure bar, (b) typical raw data collected.

Specimens were cut, grinded, and polished along the extrusion direction (ED) and impact compression direction (CD), then etched using 4.2 g picric acid, 10 mL acetic acid,

70 mL ethanol, and 10 mL distilled water. The microstructure was observed by optical microscopy (OM, OLYCIA M3, DQZH Ltd., Beijing, China) and scanning electron microscopy (SEM, JSM-6510A, JEOL, Tokyo, Japan) equipped with an energy-dispersive spectrometer (EDS). The chemical compositions of Mg-6Er and Mg-6Er-1Zn alloys measured using X-ray fluorescence (XRF) are shown in Table 1. Phase identification was performed by X-ray diffraction (XRD, Bruker D8 Discover, Bruker, Karlsruhe, Germany) using Cu K $\alpha$  radiation in the 2 $\theta$  range from 20° to 90°. The second phase and substructures were characterized using transmission electron microscopy (TEM, JEM 2100F, JEOL, Tokyo, Japan). In addition, the FEI SEM (Quanta 650, FEI Company, Hillsboro, OR, USA) equipped with an Aztec EBSD acquisition system was used to analyze the texture and grain size with a scan step of 0.4  $\mu$ m and voltage of 20 kV.

**Table 1.** The chemical composition (in wt %) of Mg-6Er and Mg-6Er-1Zn alloys.

Samples	Mg	Er	Zn	Al	Mn
Mg-6Er alloy (E6)	Bal.	5.69	-	0.05	0.01
Mg-6Er-1Zn alloy (EZ61)	Bal.	6.24	1.08	0.05	0.01

### 3. Results

#### 3.1. Microstructure and Mechanical Properties of Extruded Alloys

Figure 2 shows OM of as-cast and extruded E6 and EZ61 alloys. The average grain sizes of the as-cast E6 and EZ61 alloys are 91.3  $\mu$ m and 89.6  $\mu$ m, respectively. The as-cast alloys represent dendrite morphology, while with 1wt%Zn addition, the secondary dendrite arm spacing (SDAS) becomes smaller (see Figure 2a,b). Moreover, dynamic recrystallization occurs during extrusion, so grain refinement and more uniform microstructure can be observed, as shown in Figure 2c,d. The average grain sizes of the extruded E6 and EZ61 alloys are reduced to 11.5  $\mu$ m and 13.2  $\mu$ m, respectively.

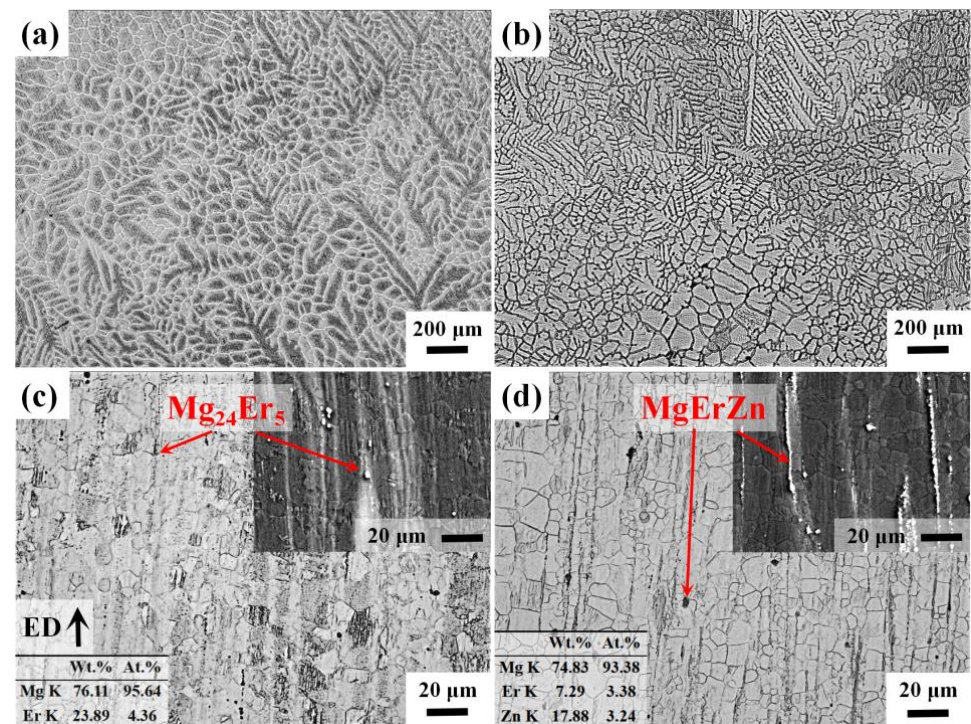


**Figure 2.** OM images of (a) as-cast E6 alloy, (b) as-cast EZ61 alloy, (c) extruded E6 alloy, and (d) extruded EZ61 alloy. The insets exhibit SEM images of different second phases distributed along the ED.

In order to distinguish the second particles during extrusion, the SEM images of both alloys are also given in the upper right insets of Figure 2c,d. Clearly, the second phases are broken and distributed along the extrusion direction (ED). With the help of EDS analysis, the second phases in E6 and EZ61 alloys were identified as  $Mg_{24}Er_5$  and  $MgErZn$  phase, respectively. Usually, in Mg-RE-Zn ternary alloys, I-phase ( $Mg_3REZn_6$ ), W-phase ( $Mg_3RE_2Zn_3$ ), and LPSO-phase alloys are typically precipitates [8]. The formation of the I phase and W phase is closely related to the ratio of Zn/RE (RE stands for elements such as Y, Er, and Ho), where a Zn/RE ratio of less than 0.8 mainly precipitates the W phase [24,25]. The Zn/Er in the EZ61 alloy is about 0.17; thus, the second phase is deduced as W phase. Simultaneously, XRD analysis was carried out to further confirm that phase.

Figure 3 shows the XRD profile of extruded E6 and EZ61 alloys. The main peak of both alloys is  $\alpha$ -Mg matrix. In the case of the extruded E6 alloy, the  $Mg_{24}Er_5$  phase cannot be identified due to its low content, while the extruded EZ61 alloy presents the W phase ( $Mg_3Zn_3Er_2$ ) diffraction peak as well as the  $\alpha$ -Mg phase. The relative content of the W phase is calculated to be only 0.486% from the reference intensity ratio (RIR) values. The index peaks of the LPSO phase do not appear when comparing the XRD results of other reported Mg-Er-Zn alloys due to the low Zn content in this study [26].

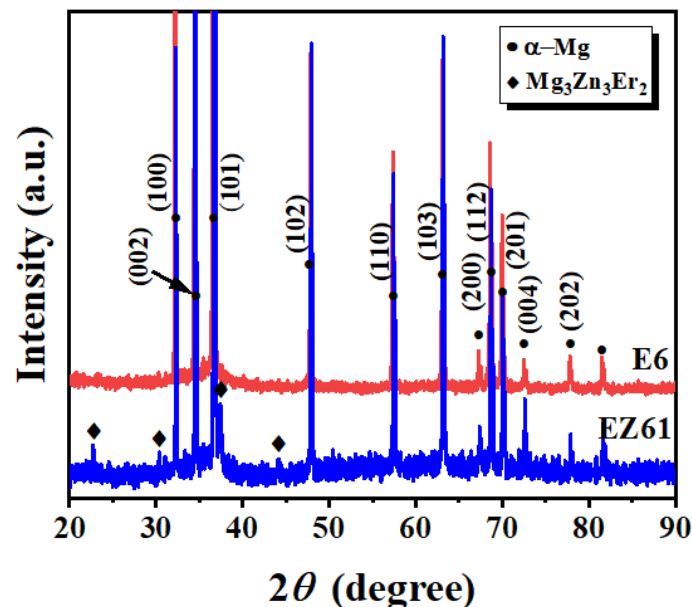
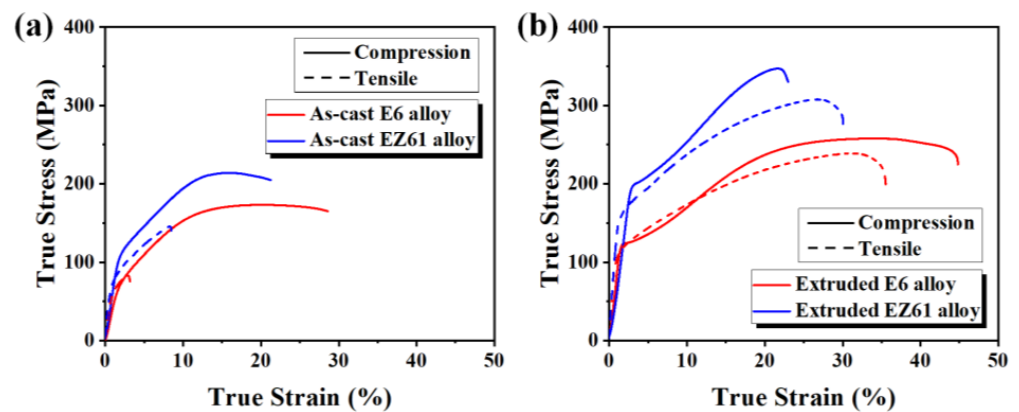


Figure 3. XRD profiles of extruded E6 and EZ61 alloys.

Figure 4 shows the true stress–strain curves (strain rate:  $0.001\text{ s}^{-1}$ ) in compression and tension for as-cast and extruded E6 and EZ61 alloys at room temperature. Table 2 shows the corresponding mechanical properties of the as-cast and extruded alloys. The compressive yield strength (CYS) and uniaxial compressive strength (UCS) of the extruded E6 alloy are 122 MPa and 258 MPa, respectively. With the addition of trace Zn elements (1 wt %) to the E6 alloy, the CYS and UCS increase to 196 MPa and 347 MPa, respectively. In addition, the tensile yield strength (TYS) and uniaxial tensile strength (UTS) of the EZ61 alloy also increased by 52.9% and 27.9% compared to the E6 alloy. Figure 5 shows the macromorphology, micromorphology, and fracture section of the extruded E6 and EZ61 alloy tensile specimens after fracture. There are many dimples in the fracture of the extruded alloy, which are densely distributed and exhibit typical ductile fracture characteristics.



**Figure 4.** True stress–strain curves of (a) as-cast and (b) extruded E6 and EZ61 alloys in compression and tension.

**Table 2.** Mechanical properties of as-cast and extruded E6 and EZ61 alloys in compression and tension.

Sample	CYS (MPa)	UCS (MPa)	TYS (MPa)	UTS (MPa)
As-cast E6 alloy	$75.5 \pm 2.2$	$174.4 \pm 3.5$	$69.3 \pm 2.1$	$83.5 \pm 2.3$
As-cast EZ61 alloy	$110.2 \pm 2.8$	$213.8 \pm 3.2$	$77.9 \pm 2.6$	$146.1 \pm 2.6$
Extruded E6 alloy	$122.1 \pm 2.7$	$257.8 \pm 4.1$	$102.2 \pm 2.5$	$239.8 \pm 2.7$
Extruded EZ61 alloy	$195.9 \pm 3.1$	$347.2 \pm 3.8$	$156.1 \pm 2.6$	$306.9 \pm 3.2$

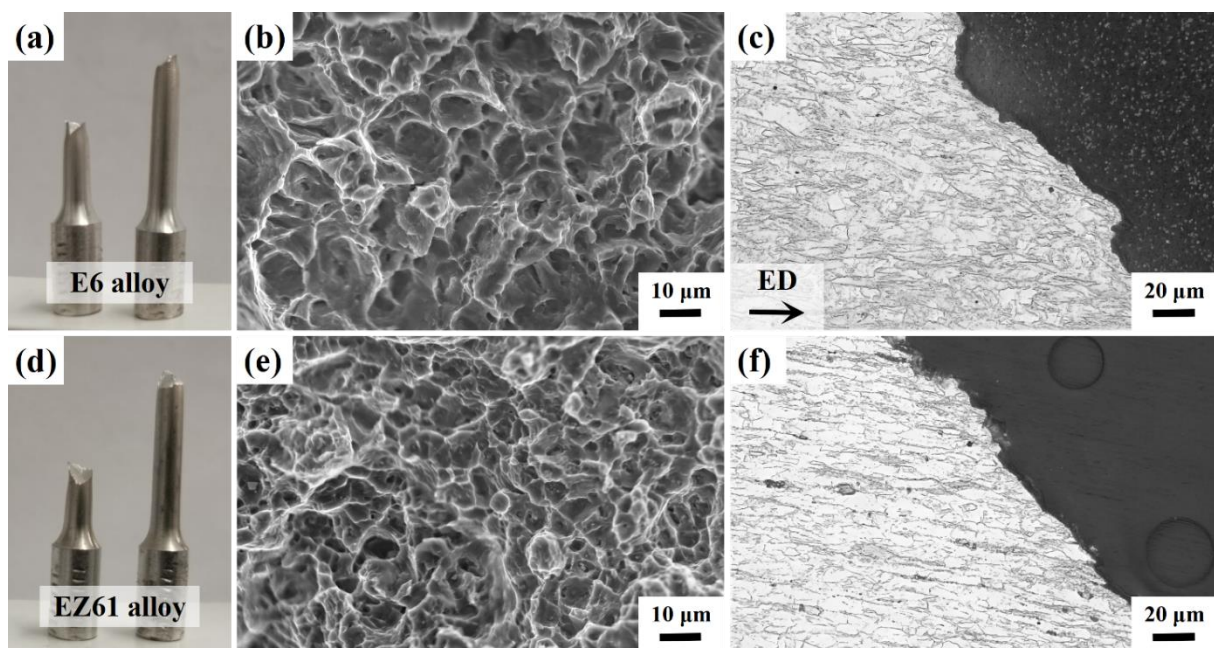


**Figure 5.** Macromorphology (a), micromorphology (b), and fracture section (c) of extruded E6 alloy tensile specimen. Macromorphology (d), micromorphology (e), and fracture section (f) of extruded EZ61 alloy tensile specimen.

TEM characterization was carried out in order to better understand the substructures and intermetallics in both E6 and EZ61 alloys, as shown in Figure 6a,b. Several precipitates of various shapes can be observed in both alloys. For instance, the second phase of E6 and EZ61 alloys is rod-shaped or partially triangular. The additional EDS analysis and selected area electron diffraction (SAED) indexing of such precipitates indicate that the second

phases are  $Mg_{24}Er_5$  and W phases, respectively. Generally, the  $Mg_{24}Er_5$  phase belongs to the body-centered cubic (BCC) structure and the W phase belongs to the face-centered cubic (FCC) structure [8,27]. In addition, stacking faults (SFs) are also found in the EZ61 alloy, 500–2000 nm in length and less than 10 nm in width, as shown in Figure 6c. However, only a clear 2H-Mg crystal structure with no extra spots was detected by the utilization of the corresponding SAED pattern (see Figure 6d). Thus, the streaks between diffraction spots along the c-axis confirm the formation of SFs rather than LPSO phases [17]. The absence of LPSO in the present EZ61 alloy may be attributed to the low Zn/Er ratio. This TEM analysis is also in agreement with the XRD and SEM results above.

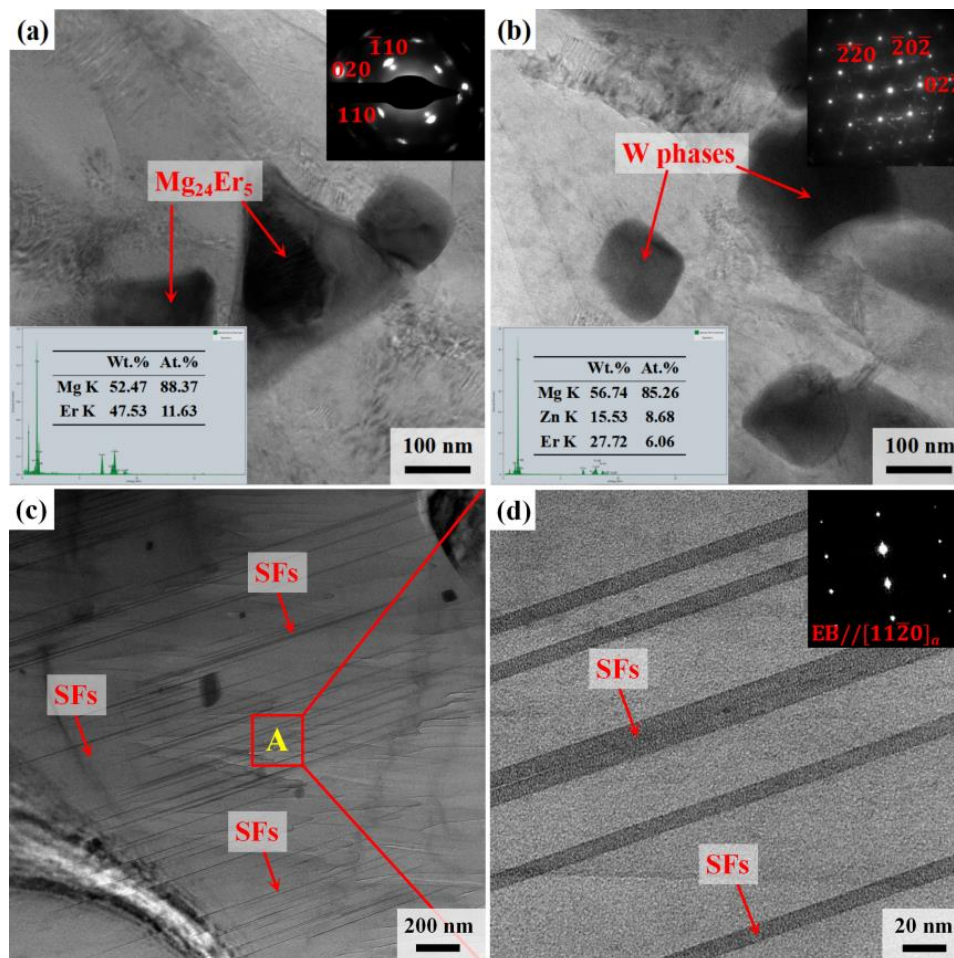


**Figure 6.** Bright field images of the second phases and their corresponding SAED patterns in (a) extruded E6 alloy and (b) EZ61 alloy; (c) numerous stacking faults (SFs) generated in EZ61 alloy; (d) enlarged view of “A” area in (c).

### 3.2. Dynamic Behavior of Mg-Er-(Zn) Alloys

In order to investigate the dynamic behavior of extruded E6 and EZ61 alloys, dynamic impact tests were carried out by SHPB. Dynamic impact responses from both E6 and EZ61 alloys at pressures of 0.15, 0.25, 0.35, and 0.45 MPa were obtained and repeated three times, representing corresponding strain rates from  $\sim 900$  to  $\sim 2500$   $s^{-1}$ . The relationship between the pressures and the average strain rate of the specimens is shown in Figure 7, where the strain rate increases linearly with increasing pressure. The strain rate of the extruded EZ61 alloy is lower than that of the E6 alloy due to its higher strength.

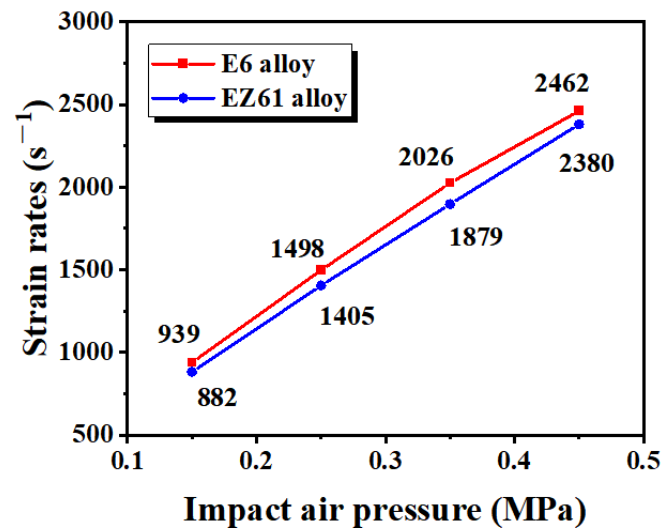


Figure 7. Strain rates of extruded E6 and EZ61 alloys at different impact air pressures.

Figure 8 shows the true compressive stress–strain curves of E6 and EZ61 alloys under various strain rates. Table 3 shows the mechanical properties of extruded E6 and EZ61 alloys in different strain rate ranges. The abnormal curves caused by uncontrollable factors (i.e., unstable pressure, broken strain gauges, and external noise) during the SHPB experiments were removed carefully. Overall, the trends under different strain rates appear similar. All the initial elastic deformation follows the Hooke’s law. Generally, the influence of the alloying elements, heat treatment, cold plastic deformation, and external factors (i.e., temperature, loading rate) on the elastic modulus are limited [28]. Therefore, in the case of high strain rates, the elastic deformation stage is similar to the quasi-static condition.

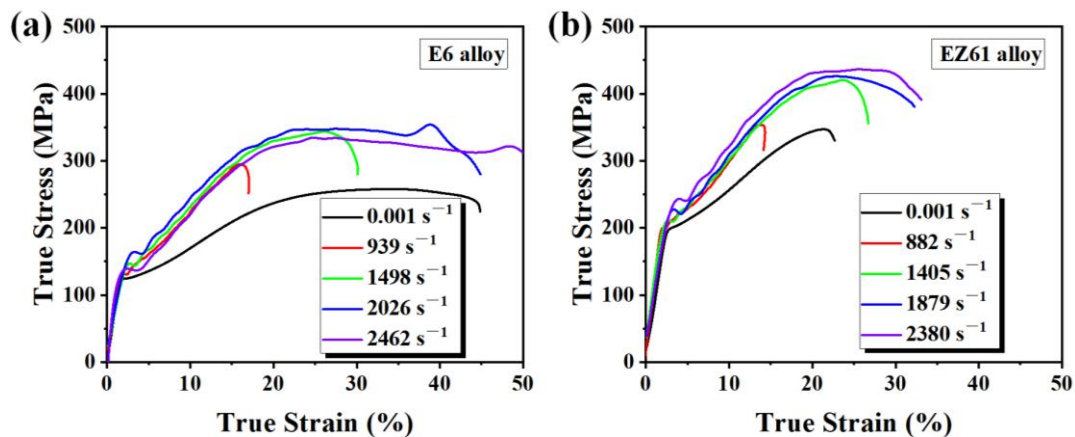


Figure 8. True stress–strain curves of extruded E6 alloy (a) and EZ61 alloy (b) at different strain rates, respectively.

Table 3. Mechanical properties of extruded E6 and EZ61 alloys in different strain rate ranges.

Strain Rates Range (s <sup>-1</sup> )	E6 Alloy		EZ61 Alloy	
	CYS (MPa)	UCS (MPa)	CYS (MPa)	UCS (MPa)
0.001	122.1 ± 2.7	257.8 ± 4.1	195.9 ± 3.1	347.2 ± 3.8
900	129.1 ± 4.2	294.5 ± 4.3	197.3 ± 3.9	352.5 ± 4.8
1450	140.4 ± 4.8	342.6 ± 3.9	208.1 ± 4.5	419.9 ± 4.1
1950	157.7 ± 5.1	354.2 ± 4.6	211.8 ± 3.8	425.7 ± 4.9
2400	134.3 ± 4.2	334.3 ± 4.5	220.2 ± 4.2	435.9 ± 5.2

Both E6 and EZ61 alloys show a yield plateau with an obvious yield point, after which the stress rises rapidly with the increasing strain, indicating a strong work hardening response. After reaching a certain strain, there is a slight drop in stress, showing stress softening due to dislocation slips. The flow stresses increase with the strain rate at the same strain in both alloys, which is typical dynamic behavior [29]. The behavior in the E6 alloy at a strain rate of  $2462 \text{ s}^{-1}$  is attributed to the competition between strain hardening and thermal softening caused by the increase in adiabatic temperature with strain rate, particularly in high strain rate deformation [30]. In addition, the yield stress increases significantly at higher strain rates with the increased strain rates. At strain rates around  $1450 \text{ s}^{-1}$ , the CYS and UCS in the E6 alloy increase by 14.7% and 32.9%, respectively, while the CYS and UCS in the EZ61 alloy increase by only 6.1% and 21.0%, respectively, compared to quasi-static circumstances.

### 3.3. Dynamic Impact Microstructure Evolution

Figure 9 shows the macroscopic morphology of the specimen after impact at various strain rates. As the strain rate increases, the thickness of the specimen becomes progressively thinner and eventually cracks. As can be seen in the figure, the fracture of the EZ61 alloy occurs at a strain rate of around  $1950 \text{ s}^{-1}$ , and E6 alloy cracking occurs at a strain rate of about  $2400 \text{ s}^{-1}$ .

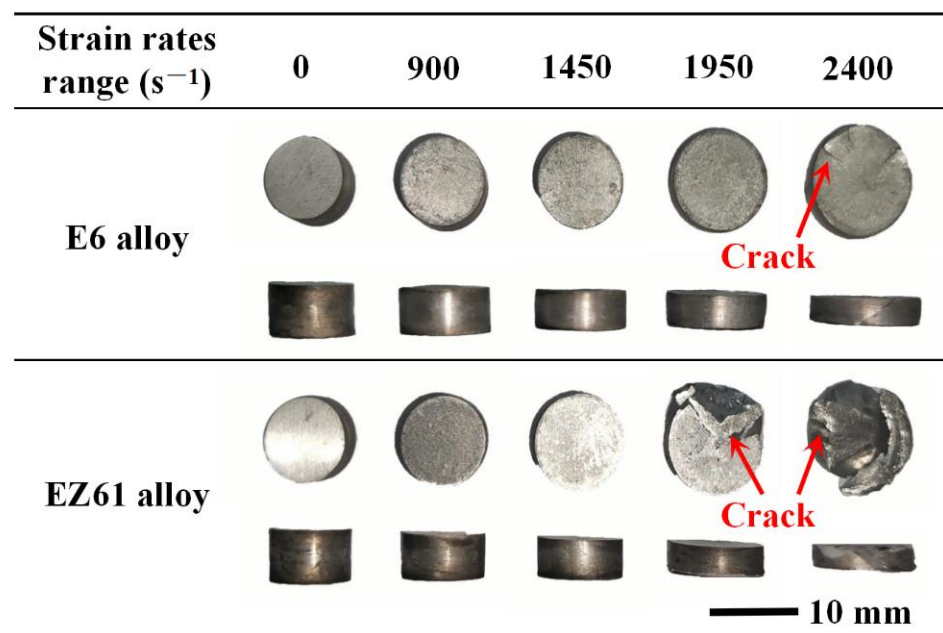


**Figure 9.** Macroscopic appearance of specimens after impact tests.

EBSD characterization was selected for the comprehensive analysis of the microstructure evolution at high strain rates of  $\sim 1450 \text{ s}^{-1}$ . Figure 10 shows the inverse pole figures (IPF), grain boundary orientation angle distribution, and grain size distribution for E6 and EZ61 alloys. In addition, Figure 11 represents HAGBs in black with a high misorientation range larger than  $15^\circ$ , LAGBs in red with a low misorientation range from  $2^\circ$  to  $15^\circ$ , and  $\{10\text{--}12\}$  tensile twin boundaries (TTBs) in green. The extruded E6 alloy contains many tension twins, with a fraction of about 35.1%, while the extruded EZ61 alloy has only 4.1% tension twins, as shown in Figures 10 and 11. The average grain boundary orientation angles for extruded E6 and EZ61 alloys are  $60.7^\circ$  and  $58.6^\circ$ , respectively, with grain boundaries consisting mainly of HAGBs and few LAGBs. Generally, the change in misorientation is closely related to the degree of recrystallization. For HAGBs accompanied by the appearance of new grains, the larger average grain boundary orientation angle indicates a higher degree of recrystallization [31]. The different colors of the IPF diagram indicate that many

recrystallized grains with random orientation occur during extrusion. The average grain size of the extruded E6 and EZ61 alloys are 11.5  $\mu\text{m}$  and 13.2  $\mu\text{m}$ , respectively. Almost no difference is found.

Moreover, the reduction in the  $\{0001\}$  basal texture after dynamic impact of the extruded E6 and EZ61 alloys can be observed in Figure 10g,j. The misorientation angle also decreases to 18.1° and 12.2° for the E6 and EZ61 alloys, respectively. Additionally, the twin volume fraction drops to 26.3% for the E6 alloy and rises to 17.0% for the EZ61 alloy after dynamic impact deformation (see Figure 11c,d). The average grain sizes of E6 and EZ61 alloys after impact tests are 9.8  $\mu\text{m}$  and 8.1  $\mu\text{m}$ , respectively, which are slightly smaller than extruded ones. In addition, more visible refinement in the EZ61 alloy with trace Zn addition is observed.

Figure 12 shows the pole figures (PFs) of E6 and EZ61 alloys. It can be seen that the extruded and SHPBed specimens show a similar texture, which is unlike the  $\{0002\}\langle 10\text{--}10\rangle$  fibrous textures in Mg-Er-Zn alloys containing the I and W phases [8,32]. In particular, the texture changes significantly after dynamic impact compression: the maximum intensity of the  $\{0001\}$  PFs widely distributed at CD, and the  $\{11\text{--}20\}$  and  $\{10\text{--}10\}$  PFs preferentially distribute along TD, similar to what was previously reported [33].

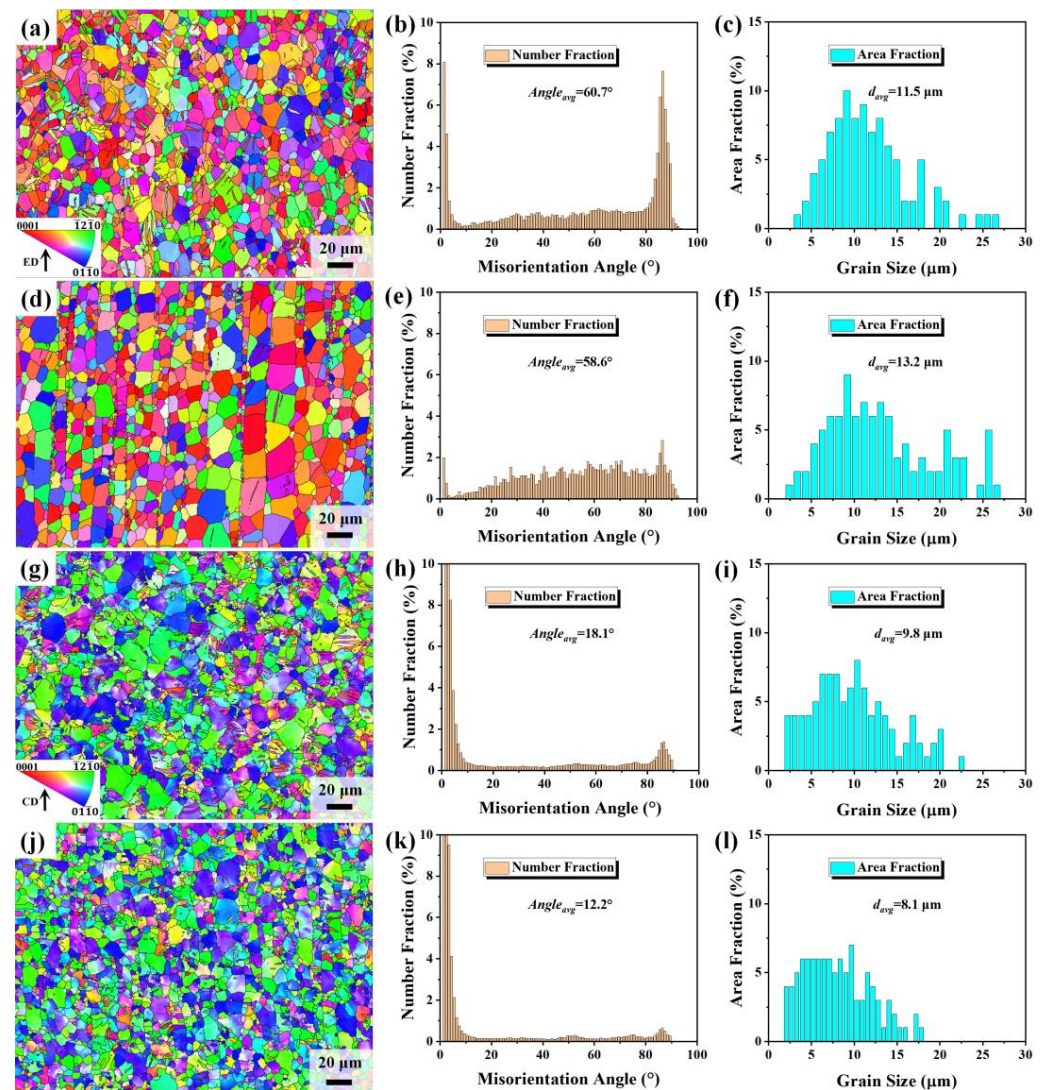


**Figure 10.** (a–f) The IPF, misorientation angle, and grain size distribution of extruded E6 and EZ61 alloys, respectively, and those of (g–l) SHPBed E6 and SHPBed EZ61 alloys, respectively. ED: extrusion direction; CD: compressive direction.

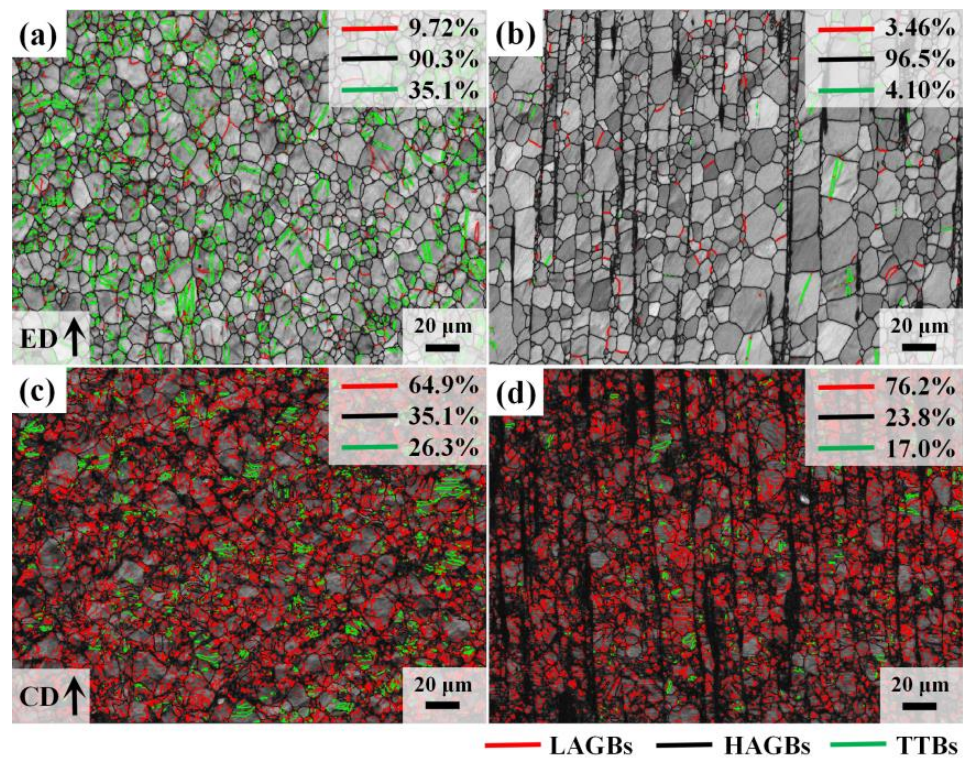


**Figure 11.** Distribution of LAGBs, HAGBs, and {10–12} twins of (a,b) extruded E6 and EZ61 alloys and (c,d) SHPBed E6 and SHPBed EZ61 alloys, respectively.

Generally, the kernel average misorientation (KAM) is high ( $>1^\circ$ ) in deformed grains due to the high density of dislocations, while KAM is low ( $<1^\circ$ ) in the recrystallized grains [34]. The KAM is usually calculated by the average misorientation to evaluate dislocation density [35,36]. The KAM calculation for a point ( $P_i$ ) calculates the directional deviation between that point and all surrounding points (each marked as  $j$ ) and then calculates the KAM value with Equation (1):

$$KAM_{P_i} = \frac{1}{N} \sum_{j=1}^N \Delta\theta_{ij}, \Delta\theta_{ij} < 5^\circ \quad (1)$$

where  $N$  is the number of surrounding points and  $\Delta\theta_{ij}$  is the orientation deviation between  $i$  and  $j$ . The KAM distribution and their average values are given in Figure 13, where the blue and green areas imply low and high dislocation densities. There are fewer substructures remaining in dynamic recrystallization (DRX) grains than in deformed ones. The DRX grains are formed at the expense of the energy storage provided by the substructure; hence, DRX grains can be defined as  $KAM < 1^\circ$  [37]. It is clear that the extruded alloys demonstrate the typical complete DRX microstructure. After SHPB tests, the dislocation density increases significantly after SHPB tests. The E6 alloy containing twins has a higher dislocation density compared to that of EZ61 alloy with SFs.

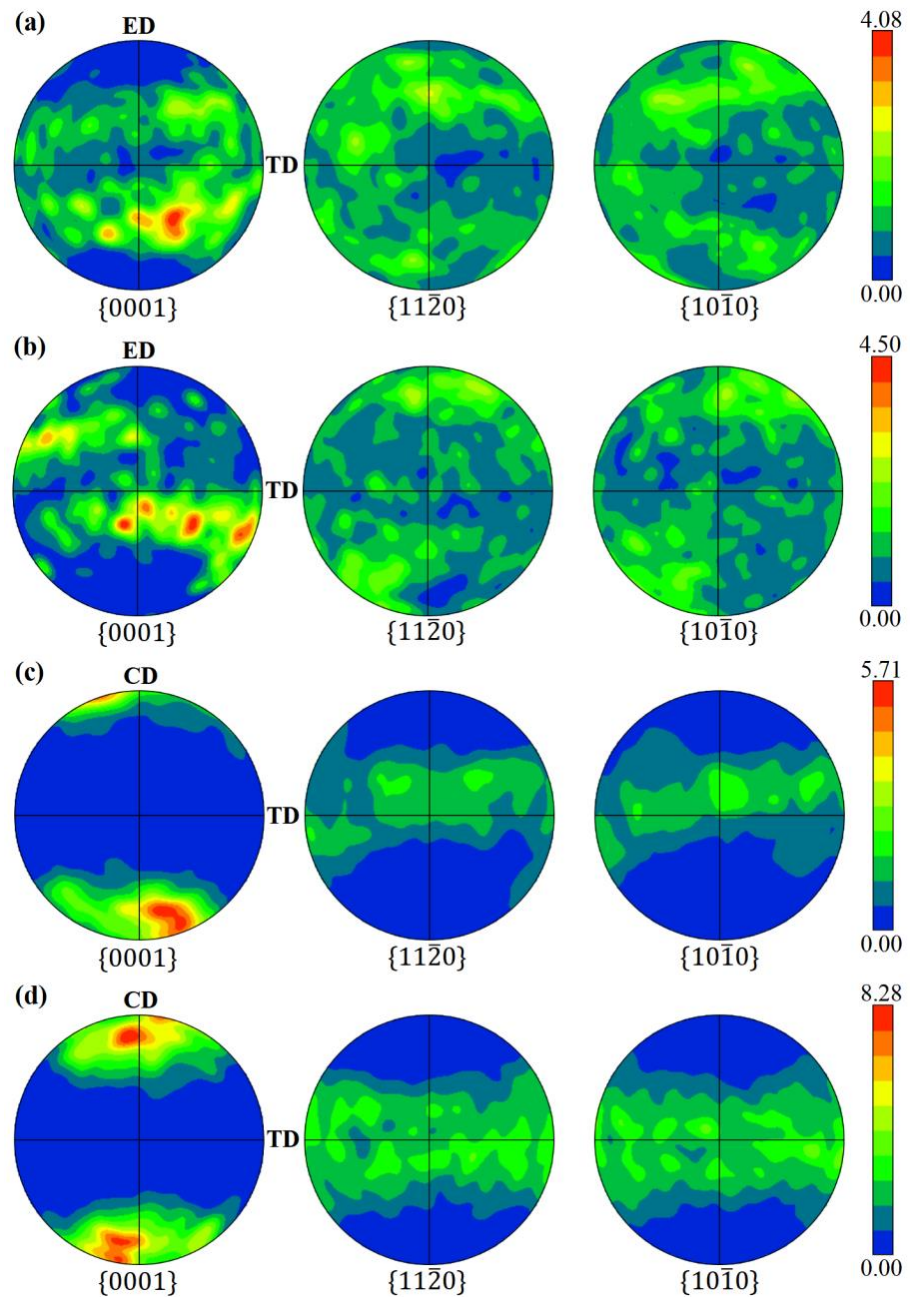


**Figure 12.** The {0001}, {11-20}, and {10-10} pole figures for (a,b) extruded E6 and EZ61 alloys and (c,d) SHPBed E6 and impact compression EZ61 alloys, respectively.

In order to detect the reason of grain refinement after SHPB tests, TEM analysis of high-speed impact alloys was carried out, as shown in Figure 14. The blue and yellow arrows in Figure 14a,b represent twin boundaries and subgrain boundaries. Simultaneously, typical dislocation cells and dislocation entanglements interacting with twins as well as SFs in deformed grains are displayed. Subgrains with LAGBs are formed gradually, and the grain refinement mechanism is discussed in the next section.

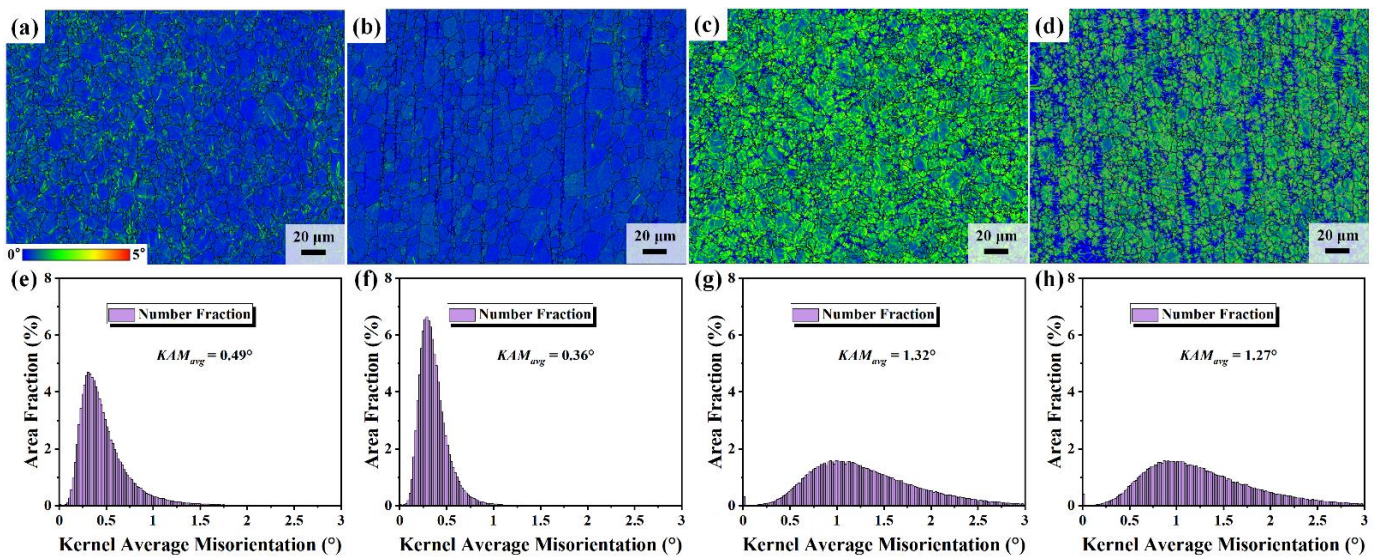


**Figure 13.** KAM maps and average KAM values of (a,e) extruded E6 alloy, (b,f) extruded EZ61 alloy, (c,g) SHPBed E6 alloy, and (d,h) SHPBed EZ61 alloy, respectively.

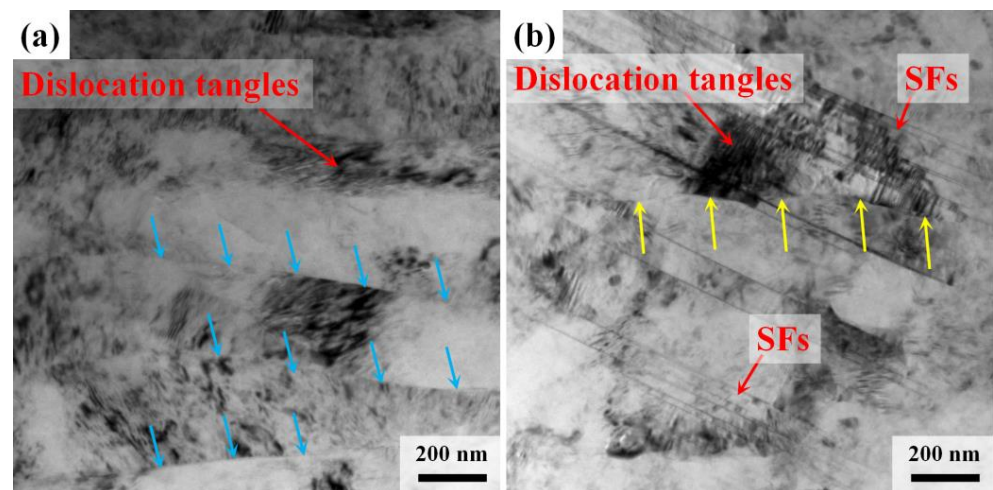


**Figure 14.** Bright field image of (a) E6 alloy and (b) EZ61 alloy after impact compression showing dislocation and stacking fault; the arrows in blue and yellow indicate twin boundary and subgrain boundary, respectively.

## 4. Discussion

### 4.1. Strengthening Mechanisms with Twins or SFs

The extruded E6 and EZ61 alloys show similar grain sizes but different flow stress responses (see Figures 8 and 10). Especially, the E6 alloy contains a large number of twins and the EZ61 alloy contains many fine SFs (see Figures 11 and 14). As the low content of the second phase in the extruded alloy has less influence on the behavior of the alloy, the main reason for the difference in the mechanical behavior of the E6 and EZ61 alloys is the generation of SFs in the EZ61 alloy. In addition, SFs can hinder the movement of twin boundaries and effectively reduce the twin volume fraction. Some other scholars also confirmed these results. Zhang et al. [38] investigated through a molecular dynamics study that SFs, as a type of planar defect, were able to retard the evaluation of {10–12} twin boundaries from the viewpoint of twin volume fraction, showing their strengthening effects on the {10–12} twins.

The extruded E6 and EZ61 alloys exhibit a relatively weak basal texture, which may be due to the discontinuous dynamic recrystallization (DDRX). As the crystalline orientation of the DDRX nuclei is independent of the original deformed grains, the new grains form a weaker texture by DDRX [39,40]. The increase in the intensity of the texture from 4.08 to 4.50 in extruded alloys with trace addition of Zn elements is due to the formation of a thermally stable Mg-Zn-Er intermetallic distributed along the ED.

The diversity between the quasi-static compressive and tensile properties of E6 and EZ61 alloys is also significant (see Figure 4). Typically, basal slip and tensile twinning are easily activated during deformation [41,42]. Tensile twins dominate during initial plastic deformation and can be thought of as 3D “faults”, where the tensile twin boundary prevents the migration of dislocations [43–45]. The SFs are formed by the copolymerization of rare earth elements and zinc, and co-growth with the  $\alpha$ -Mg matrix along the basal plane, similar to the growth mechanism of amplitude modulation decomposition [46]. Upon external stresses, SFs tend to interact with dislocations, leading to the enhancement of the strength [47–50]. In addition, the ductility of the EZ61 alloy is better than the commercial AZ61 alloy with similar yield and tensile strength [51,52], because it is easy to form the  $Mg_{17}Al_{12}$  precipitates in Mg-Al alloys. Meanwhile, the solid solution of aluminum in Mg alloys is further reduced with the addition of low amounts of Zn. Although  $Mg_{17}Al_{12}$  has a strengthening effect as a brittle phase, the ductility of the alloy decreases with the increase in the volume fraction of the  $Mg_{17}Al_{12}$  phase [53]. Simultaneously, SFs in the EZ61 alloy are effective at accumulating dislocations, which increase the strain hardening rate and maintain excellent ductility [48,49]. The addition of trace amounts of Zn or/and Er plays a key role in the modification of the weave structure and the precipitation of the nano-second phase, too [50,54]. Although both twins and SFs have a hindering effect on dislocation slip, the number of twins in a grain is limited, with only twin boundaries interacting with dislocations, whereas a large number of SFs embedded grains can interact with more dislocations. As a result, the formation of SFs impacted dislocation sliding, and in turn, increased strength in the extruded EZ61 alloy can be imaged.

#### 4.2. Dynamic Mechanical Behavior

The dynamic true stress–strain curve changes of E6 and EZ61 alloys are relatively consistent (see Figure 8). The alloy deformation strain reaches the yield point at about 3%. When the strain is between 3% and 15%, work hardening is caused by the accumulation of dislocation slip, and as the flow stress continues to increase with increasing strain, the presence of SFs significantly improves the dynamic mechanical properties of the alloy. After the deformation strain exceeds 15%, the temperature of the alloy increases due to the deformation and competition between strain hardening and thermal softening that occurred in the E6 and EZ61 alloys. With the flow stress increasing slowly, the E6 alloy will be more affected by the adiabatic temperature rise. When the deformation strain reaches about 24%, the alloy stress reaches its peak and gradually decreases with increasing deformation strain until the alloy sample fractures. The alloy work hardening rate increases after dynamic impact and the deformation stress increases with the strain rate, showing a certain strain rate hardening effect, which is typical dynamic behavior of the material [29].

The impedance influence of SFs on dislocation slip within the EZ61 alloy resists alloy deformation, resulting in higher alloy strength. The anomalous mechanical behavior of E6 alloys, where the plastic deformation stress is lower at a strain rate of  $2462\text{ s}^{-1}$  than at a strain rate of  $2026\text{ s}^{-1}$ , is due to the higher thermal softening effect than the strain hardening effect caused by the increase in adiabatic temperature with strain rate during the deformation of E6 alloys. The adiabatic temperature rise phenomenon occurs in most metal materials during high-speed deformation [55]. On the other hand, SFs are thermally stable and are less affected by adiabatic temperature rise [14].

#### 4.3. Refinement Mechanisms by SFs at High Strain Rates

Figures 11 and 13 exhibit an increase in the proportion of LAGBs in impact-compressed alloys. The increase in sub-grain and the presence of a large number of dislocations in such alloys represent a high level of distortion energy. Comparing quasi-static CYS and UCS values at the same strain rate, those of the E6 alloy vary to a greater extent than those of the EZ61 alloy (see Table 3). To the best of our knowledge, the stacking fault energy (SFE) of magnesium alloys is in the range of 60–78 mJ/m<sup>2</sup> and the simultaneous addition of Zn and RE can reduce the SFE of Mg alloys [10,47]. There are two factors that control the grain refinement process in metal, namely, the SFE and the number of slip systems [56]. During deformation, both twins and SFs hinder dislocation slip, but the EZ61 alloy has lower lamination energy than the E6 alloy, and dislocations aggregate to form LAGBs and release energy. As a result, the EZ61 alloy is more susceptible to stress-driven movement of the LAGBs to increase the dislocation orientation angle to form HAGBs and refine the grain.

Sun et al. [57] used surface mechanical abrasive treatment (SMAT) to reveal that the grain refinement process of WE43 magnesium alloys consisted of three transitional stages: dislocation cell and stacking, ultrafine subgrain, and randomly oriented nanoparticles. Moreover, Liu et al. [58] found that dislocations formed LAGBs at high strain rates by compressing steel with a shock wave generated by an air gun, and that LAGBs tended to transform into HAGBs accompanied by grain rotation. The SFs are more effective for dislocation accumulation and blocking [16]. After deformation dislocation entanglement rearrangement to form LAGBs, the movement of LAGBs driven by external stress increases the dislocation angle and forms HAGBs. Thus, the grain of the EZ61 alloy is significantly refined compared with the E6 alloy after SHPB tests.

## 5. Conclusions

Dynamic impact experiments were carried out by SHPB on extruded Mg-6Er (E6) and Mg-6Er-1Zn (EZ61) alloys under strain rates from 900 to 2500 s<sup>-1</sup>, and the microstructural evolution and related strain-stress behavior of extruded alloys and impact-compressed alloys were systemically investigated. The addition of Zn in Mg-Er resulted in profuse SFs, which interacted with dislocations and hindered their sliding, thus increasing the compressive and tensile strength of the EZ61 alloy. The flow stress of both alloys increased with the increasing strain rate, showing a strain rate hardening effect. In addition, the addition of Zn and Er elements reduced the laminar dislocation energy and LAGBs in the EZ61 alloy, which was more likely to form HAGBs.

**Author Contributions:** Conceptualization, H.Y. and W.Y.; methodology, H.Y., J.R., S.K. and W.Y.; formal analysis, H.Y., J.R. and W.Y.; investigation, S.K., Z.W., J.F., Q.W. and P.J.; resources, Z.W., J.F., Q.W., P.J., X.Z. and F.Y.; writing—original draft preparation, H.Y. and J.R.; writing—review and editing, H.Y., J.R., S.K., W.Y., Z.W., J.F., Q.W., P.J., X.Z. and F.Y.; and project administration, H.Y. All authors have read and agreed to the published version of the manuscript.

**Funding:** This work was supported by the National Natural Science Foundation of China (No. 51701060) and the Scientific Research Foundation for the Returned Overseas Chinese Scholars of Hebei Province (No. C20190505) under the Hebei Provincial Key Research Special Project “Development and Application of Key Preparation Technology of High Strength and Toughness Magnesium Alloys for Automobile Wheel Hub” from Hebei Development and Reform Commission and Hebei Provincial Department of Finance, China.

**Institutional Review Board Statement:** Not applicable.

**Informed Consent Statement:** Not applicable.

**Data Availability Statement:** Not applicable.

**Conflicts of Interest:** The authors declare no conflict of interest.

## References

1. Xu, T.C.; Yang, Y.; Peng, X.D.; Song, J.F.; Pan, F.S. Overview of advancement and development trend on magnesium alloy. *J. Magnes. Alloys* **2019**, *7*, 536–544. [\[CrossRef\]](#)
2. Li, J.L.; Wu, D.; Chen, R.S.; Han, E.H. Anomalous effects of strain rate on the room-temperature ductility of a cast Mg-Gd-Y-Zr alloy. *Acta Mater.* **2018**, *159*, 31–45. [\[CrossRef\]](#)
3. Feng, F.; Huang, S.Y.; Meng, Z.H.; Hu, J.H.; Lei, Y.; Zhou, M.C.; Wu, D.; Yang, Z.Z. Experimental study on tensile property of AZ31B magnesium alloy at different high strain rates and temperatures. *Mater. Des.* **2014**, *57*, 10–20. [\[CrossRef\]](#)
4. Tang, W.R.; Liu, Z.; Liu, S.M.; Zhou, L.; Mao, P.L.; Guo, H.; Sheng, X.F. Deformation mechanism of fine grained Mg-7Gd-5Y-1.2Nd-0.5Zr alloy under high temperature and high strain rates. *J. Magnes. Alloys* **2020**, *8*, 1144–1153. [\[CrossRef\]](#)
5. Li, A.W.; Li, W.; Luo, M.; Yu, H.M.; Sun, Y.D.; Liang, Y.L. Effect of grain size on the microstructure and deformation mechanism of Mg-2Y-0.6Nd-0.6Zr alloy at a high strain rate. *Mater. Sci. Eng. A* **2021**, *824*, 141774. [\[CrossRef\]](#)
6. Tang, W.R.; Liu, S.M.; Liu, Z.; Kang, S.; Mao, P.L.; Zhou, L.; Wang, Z. Microstructure evolution and constitutive relation establishment of Mg-7Gd-5Y-1.2Nd-0.5Zr alloy under high strain rate after severe multi-directional deformation. *Mater. Sci. Eng. A* **2021**, *809*, 140994. [\[CrossRef\]](#)
7. Liu, Y.Y.; Mao, P.L.; Zhang, F.; Liu, Z.; Wang, Z. Effect of temperature on the anisotropy of AZ31 magnesium alloy rolling sheet under high strain rate deformation. *Philos. Mag.* **2018**, *98*, 1068–1086. [\[CrossRef\]](#)
8. Liu, K.; Sun, C.C.; Wang, Z.H.; Li, S.B.; Wang, Q.F.; Du, W.B. Microstructure, texture and mechanical properties of Mg-Zn-Er alloys containing I-phase and W-phase simultaneously. *J. Alloys Compd.* **2016**, *665*, 76–85. [\[CrossRef\]](#)
9. Tahreen, N.; Zhang, D.F.; Pan, F.S.; Jiang, X.Q.; Li, D.Y.; Chen, D.L. Strengthening mechanisms in magnesium alloys containing ternary I, W and LPSO phases. *J. Mater. Sci. Technol.* **2018**, *34*, 1110–1118. [\[CrossRef\]](#)
10. Yamasaki, M.; Sasaki, M.; Nishijima, M.; Hiraga, K.; Kawamura, Y. Formation of 14H long period stacking ordered structure and profuse stacking faults in Mg-Zn-Gd alloys during isothermal aging at high temperature. *Acta Mater.* **2007**, *55*, 6798–6805. [\[CrossRef\]](#)
11. Li, D.J.; Zeng, X.Q.; Dong, J.; Zhai, C.Q.; Ding, W.J. Microstructure evolution of Mg-10Gd-3Y-1.2Zn-0.4Zr alloy during heat-treatment at 773 K. *J. Alloys Compd.* **2009**, *468*, 164–169. [\[CrossRef\]](#)
12. Shao, X.H.; Yang, Z.Q.; Ma, X.L. Strengthening and toughening mechanisms in Mg-Zn-Y alloy with a long period stacking ordered structure. *Acta Mater.* **2010**, *58*, 4760–4771. [\[CrossRef\]](#)
13. Zhang, L.; Zhang, J.H.; Xu, C.; Jing, Y.B.; Zhuang, J.P.; Wu, R.Z.; Zhang, M.L. Formation of stacking faults for improving the performance of biodegradable Mg-Ho-Zn alloy. *Mater. Lett.* **2014**, *133*, 158–162. [\[CrossRef\]](#)
14. Xu, C.; Zhang, J.H.; Liu, S.J.; Jing, Y.B.; Jiao, Y.F.; Xu, L.J.; Zhang, L.; Jiang, F.C.; Zhang, M.L.; Wu, R.Z. Microstructure, mechanical and damping properties of Mg-Er-Gd-Zn alloy reinforced with stacking faults. *Mater. Des.* **2015**, *79*, 53–59. [\[CrossRef\]](#)
15. Jiao, Y.F.; Zhang, J.H.; Jing, Y.B.; Xu, C.; Liu, S.J.; Zhang, L.; Xu, L.J.; Zhang, M.L.; Wu, R.Z. Development of High-Performance Mg Alloy via Introducing Profuse Long Period Stacking Ordered Phase and Stacking Faults. *Adv. Eng. Mater.* **2015**, *17*, 876–884. [\[CrossRef\]](#)
16. Jian, W.W.; Cheng, G.M.; Xu, W.Z.; Yuan, H.; Tsai, M.H.; Wang, Q.D.; Koch, C.C.; Zhu, Y.T.; Mathaudhu, S.N. Ultrastrong Mg Alloy via Nano-spaced Stacking Faults. *Mater. Res. Lett.* **2013**, *1*, 61–66. [\[CrossRef\]](#)
17. Jiao, Y.F.; Zhang, J.H.; Kong, P.Y.; Zhang, Z.W.; Jing, Y.B.; Zhuang, J.P.; Wang, W.; Zhang, L.; Xu, C.; Wu, R.Z.; et al. Enhancing the performance of Mg-based implant materials by introducing basal plane stacking faults. *J. Mater. Chem. B* **2015**, *3*, 7386–7400. [\[CrossRef\]](#)
18. Wang, M.; Xu, X.Y.; Wang, H.Y.; He, L.H.; Huang, M.X. Evolution of dislocation and twin densities in a Mg alloy at quasi-static and high strain rates. *Acta Mater.* **2020**, *201*, 102–113. [\[CrossRef\]](#)
19. Zhang, F.; Liu, Z.; Wang, Y.; Mao, P.L.; Kuang, X.W.; Zhang, Z.L.; Ju, Y.D.; Xu, X.Z. The modified temperature term on Johnson-Cook constitutive model of AZ31 magnesium alloy with {0002} texture. *J. Magnes. Alloys* **2020**, *8*, 172–183. [\[CrossRef\]](#)
20. Zhao, F.; Suo, T.; Chen, B.; Li, Y.L. Strength-ductility combination of fine-grained magnesium alloy with high deformation twin density. *J. Alloys Compd.* **2019**, *798*, 350–359. [\[CrossRef\]](#)
21. Guo, P.C.; Li, L.X.; Xiao, G.; Cao, S.F.; Wang, G.; He, H. High-speed impact behavior of a casting AM80 magnesium alloy under various deformation temperatures. *J. Alloys Compd.* **2019**, *811*, 151875. [\[CrossRef\]](#)
22. Guo, P.C.; Tang, Q.; Li, L.X.; Xie, C.; Liu, W.H.; Zhu, B.W.; Liu, X. The deformation mechanism and adiabatic shearing behavior of extruded Mg-8.0Al-0.1Mn alloy in different heat treated states under high-speed impact load. *J. Mater. Res. Technol.* **2021**, *11*, 2195–2207. [\[CrossRef\]](#)
23. Zhu, C.C.; Song, Y.T.; Peng, X.B.; Wei, Y.P.; Mao, X.; Li, W.X.; Qian, X.Y. The dynamical mechanical properties of tungsten under compression at working temperature range of divertors. *J. Nucl. Mater.* **2016**, *469*, 120–124. [\[CrossRef\]](#)
24. Li, H.; Du, W.B.; Li, S.B.; Wang, Z.H. Effect of Zn/Er weight ratio on phase formation and mechanical properties of as-cast Mg-Zn-Er alloys. *Mater. Des.* **2012**, *35*, 259–265. [\[CrossRef\]](#)
25. Xu, D.K.; Liu, L.; Xu, Y.B.; Han, E.H. The influence of element Y on the mechanical properties of the as-extruded Mg-Zn-Y-Zr alloys. *J. Alloys Compd.* **2006**, *426*, 155–161. [\[CrossRef\]](#)
26. Wen, K.; Qin, Z.; Li, Y.; Zhang, W. Effect of heat treatment on structure transformation of LPSO phase of Mg-Er-Zn(Zr) alloy. *Ordnance Mater. Sci. Eng.* **2018**, *41*, 74–78.

27. Wang, Z.J.; Jia, W.P.; Cui, J.Z. Study on the deformation behavior of Mg-3.6%Er magnesium alloy. *J. Rare Earths* **2007**, *25*, 744–748.
28. Yang, Z.J.; Cao, J.H.; Yu, W.X.; Hou, S.S.; Wang, G.L.; Lang, S.T.; Ding, P. Effects of microstructure characteristics on the mechanical properties and elastic modulus of a new Ti-6Al-2Nb-2Zr-0.4B alloy. *Mater. Sci. Eng. A* **2021**, *820*, 141564. [[CrossRef](#)]
29. Qian, X.Y.; Peng, X.B.; Song, Y.T.; Huang, J.J.; Wei, Y.P.; Liu, P.; Mao, X.; Zhang, J.W.; Wang, L. Dynamic constitutive relationship of CuCrZr alloy based on Johnson-Cook model. *Nucl. Mater. Energy* **2020**, *24*, 100768. [[CrossRef](#)]
30. Abd El-Aty, A.; Xu, Y.; Zhang, S.H.; Ha, S.; Ma, Y.; Chen, D.Y. Impact of high strain rate deformation on the mechanical behavior, fracture mechanisms and anisotropic response of 2060 Al-Cu-Li alloy. *J. Adv. Res.* **2019**, *18*, 19–37. [[CrossRef](#)]
31. Gui, Y.W.; Ouyang, L.X.; Cui, Y.J.; Bian, H.K.; Li, Q.A.; Chiba, A. Grain refinement and weak-textured structures based on the dynamic recrystallization of Mg-9.80Gd-3.78Y-1.12Sm-0.48Zr alloy. *J. Magnes. Alloys* **2021**, *9*, 456–466. [[CrossRef](#)]
32. Wang, Q.F.; Liu, K.; Wang, Z.H.; Li, S.B.; Du, W.B. Microstructure, texture and mechanical properties of as-extruded Mg-Zn-Er alloys containing W-phase. *J. Alloys Compd.* **2014**, *602*, 32–39. [[CrossRef](#)]
33. Yu, H.; Liu, H.; Jiang, B.N.; Yu, W.; Kang, S.M.; Cheng, W.L.; Park, S.; Chen, D.; Yin, F.X.; Shin, K.; et al. A Comprehensive Study of Dynamic Recrystallization Behavior of Mg Alloy with 3 wt.% Bi Addition. *Metals* **2021**, *11*, 2838. [[CrossRef](#)]
34. Li, H.L.; Hsu, E.; Szpunar, J.; Utsunomiya, H.; Sakai, T. Deformation mechanism and texture and microstructure evolution during high-speed rolling of AZ31B Mg sheets. *J. Mater. Sci.* **2008**, *43*, 7148–7156. [[CrossRef](#)]
35. Zhang, J.Y.; Xu, B.; Tariq, N.U.; Sun, M.Y.; Li, D.A.Z.; Li, Y.Y. An innovative approach for grain refinement in Ni-based superalloys: Modification in the classical delta process through gamma “pre-aging treatment. *J. Alloys Compd.* **2020**, *818*, 152827. [[CrossRef](#)]
36. Yang, Y.; Huo, Q.H.; Zhang, Y.X.; Luo, L.; Xiao, Z.Y.; Wang, J.; Hashimoto, A.; Yang, X.Y. Effects of volume fraction of fine grains on the tensile creep properties of a hot-deformed Mg-Gd-Y-Zr alloy. *Mater. Sci. Eng. A* **2020**, *777*, 139052. [[CrossRef](#)]
37. Sakai, T.; Belyakov, A.; Kaibyshev, R.; Miura, H.; Jonas, J.J. Dynamic and post-dynamic recrystallization under hot, cold and severe plastic deformation conditions. *Prog. Mater. Sci.* **2014**, *60*, 130–207. [[CrossRef](#)]
38. Zhang, J.; Dou, Y.; Wan, X.; Chen, J. The strengthening effects of basal stacking faults on {10–12} twin in magnesium: A molecular dynamics study. *Comput. Condens. Matter* **2020**, *23*, e00466. [[CrossRef](#)]
39. Fonda, R.W.; Knipling, K.E. Texture development in friction stir welds. *Sci. Technol. Weld. Join.* **2011**, *16*, 288–294. [[CrossRef](#)]
40. Jiang, M.G.; Xu, C.; Yan, H.; Fan, G.H.; Nakata, T.; Lao, C.S.; Chen, R.S.; Kamado, S.; Han, E.H.; Lu, B.H. Unveiling the formation of basal texture variations based on twinning and dynamic recrystallization in AZ31 magnesium alloy during extrusion. *Acta Mater.* **2018**, *157*, 53–71. [[CrossRef](#)]
41. Wang, M.; Lu, L.; Li, C.; Xiao, X.H.; Zhou, X.M.; Zhu, J.; Luo, S.N. Deformation and spallation of a magnesium alloy under high strain rate loading. *Mater. Sci. Eng. A* **2016**, *661*, 126–131. [[CrossRef](#)]
42. Zhang, W.G.; Ye, Y.C.; He, L.J.; Li, P.J.; Zhang, H.S. Dynamic mechanical response and microstructural evolution of extruded Mg AZ31B plate over a wide range of strain rates. *J. Alloys Compd.* **2017**, *696*, 1067–1079. [[CrossRef](#)]
43. Shi, D.F.; Wang, C.Y.; Cepeda-Jimenez, C.M.; Perez-Prado, M.T. Atomic scale interactions of basal dislocations and twin boundaries with ultrathin precipitates in magnesium alloys. *Acta Mater.* **2021**, *221*, 117442. [[CrossRef](#)]
44. Lv, B.J.; Wang, S.; Cui, N.; Guo, F. Twinning and dynamic recrystallization of Mg-7Sn-3Zn alloy under high strain rate hot compression. *Mater. Sci. Eng. A* **2021**, *809*, 140986. [[CrossRef](#)]
45. Luque, A.; Ghazisaeidi, M.; Curtin, W.A. A new mechanism for twin growth in Mg alloys. *Acta Mater.* **2014**, *81*, 442–456. [[CrossRef](#)]
46. Zhu, Y.M.; Morton, A.J.; Nie, J.F. Growth and transformation mechanisms of 18R and 14H in Mg-Y-Zn alloys. *Acta Mater.* **2012**, *60*, 6562–6572. [[CrossRef](#)]
47. Xu, C.; Nakata, T.; Qiao, X.G.; Zheng, M.Y.; Wu, K.; Kamado, S. Effect of LPSO and SFs on microstructure evolution and mechanical properties of Mg-Gd-Y-Zn-Zr alloy. *Sci. Rep.* **2017**, *7*, 40846. [[CrossRef](#)]
48. Bi, G.L.; Fang, D.Q.; Zhao, L.; Lian, J.S.; Jiang, Q.; Jiang, Z.H. An elevated temperature Mg-Dy-Zn alloy with long period stacking ordered phase by extrusion. *Mater. Sci. Eng. A* **2011**, *528*, 3609–3614. [[CrossRef](#)]
49. Wei, K.; Xiao, L.R.; Gao, B.; Li, L.; Liu, Y.; Ding, Z.G.; Liu, W.; Zhou, H.; Zhao, Y.H. Enhancing the strain hardening and ductility of Mg-Y alloy by introducing stacking faults. *J. Magnes. Alloys* **2020**, *8*, 1221–1227. [[CrossRef](#)]
50. Zou, G.D.; Cai, X.C.; Fang, D.Q.; Wang, Z.; Zhao, T.S.; Peng, Q.M. Age strengthening behavior and mechanical properties of Mg-Dy based alloys containing LPSO phases. *Mater. Sci. Eng. A* **2015**, *620*, 10–15. [[CrossRef](#)]
51. Jordon, J.B.; Gibson, J.B.; Horstemeyer, M.F.; El Kadiri, H.; Baird, J.C.; Luo, A.A. Effect of twinning, slip, and inclusions on the fatigue anisotropy of extrusion-textured AZ61 magnesium alloy. *Mater. Sci. Eng. A* **2011**, *528*, 6860–6871. [[CrossRef](#)]
52. Huang, H.; Huang, W.G. Study on Dynamic Mechanical Properties of Magnesium Alloy AZ61. *J. Mater. Eng.* **2009**, *117*, 51–54.
53. Asgari, H.; Szpunar, J.A.; Odeshi, A.G. Texture evolution and dynamic mechanical behavior of cast AZ magnesium alloys under high strain rate compressive loading. *Mater. Des.* **2014**, *61*, 26–34. [[CrossRef](#)]
54. Liu, K.; Liang, J.T.; Du, W.B.; Li, S.B.; Wang, Z.H.; Yu, Z.J.; Liu, J.X. Microstructure, mechanical properties and stretch formability of as-rolled Mg alloys with Zn and Er additions. *Rare Met.* **2021**, *40*, 2179–2187. [[CrossRef](#)]
55. Yan, N.; Li, Z.Z.; Xu, Y.B.; Meyers, M.A. Shear localization in metallic materials at high strain rates. *Prog. Mater. Sci.* **2021**, *119*, 100755. [[CrossRef](#)]
56. Sun, H.Q.; Shi, Y.N.; Zhang, M.A.; Lu, K. Plastic strain-induced grain refinement in the nanometer scale in a Mg alloy. *Acta Mater.* **2007**, *55*, 975–982. [[CrossRef](#)]

- 
57. Sun, W.T.; Wu, B.; Fu, H.; Yang, X.S.; Qiao, X.G.; Zheng, M.Y.; He, Y.; Lu, J.; Shi, S.Q. Combining gradient structure and supersaturated solid solution to achieve superior mechanical properties in WE43 magnesium alloy. *J. Mater. Sci. Technol.* **2022**, *99*, 223–238. [[CrossRef](#)]
  58. Liu, Q.; Fang, L.M.; Xiong, Z.W.; Yang, J.; Tan, Y.; Liu, Y.; Zhang, Y.J.; Tan, Q.; Hao, C.C.; Cao, L.H.; et al. The response of dislocations, low angle grain boundaries and high angle grain boundaries at high strain rates. *Mater. Sci. Eng. A* **2021**, *822*, 141704. [[CrossRef](#)]